The VMC survey – XXXV. model fitting of LMC Cepheid light curves

Fabio Ragosta,[1,2,3] Marcella Marconi,[3] Roberto Molinaro,[3]* Vincenzo Ripepi,[3]
Maria Rosa L. Cioni,[4] Maria Ida Moretti,[3] Martin A. T. Groenewegen,[5]
Samyaday Choudhury,[6,7] Richard de Grijs,[6,7,8] Jacco Th. van Loon,[9]
Joana M. Oliveira [9], Valentin D. Ivanov[10] and Carlos Gonzalez-Fernandez [11]

[1]*Dipartimento di Fisica, Via Cinthia, I-80126 Fuorigrotta, Naples, Italy*
[2]*INFN sez. di Napoli Compl. Univ. di Monte S. Angelo, Edificio G, Via Cinthia, I-80126 Napoli, Italy*
[3]*INAF-Osservatorio Astronomico di Capodimonte, via Moiariello 16, I-80131 Naples, Italy*
[4]*Leibniz-Institut für Astrophysik Potsdam, An der Sternwarte 16, D-14482 Potsdam, Germany*
[5]*Koninklijke Sterrenwacht van België, Ringlaan 3, B-1180 Brussels, Belgium*
[6]*Department of Physics and Astronomy, Macquarie University, Balaclava Road, Sydney, NSW 2109, Australia*
[7]*Research Centre for Astronomy, Astrophysics and Astrophotonics, Macquarie University, Balaclava Road, Sydney, NSW 2109, Australia*
[8]*International Space Science Institute–Beijing, 1 Nanertiao, Zhongguancun, Hai Dian District, 100190 Beijing, PR China*
[9]*Lennard-Jones Laboratories, School of Chemical and Physical Sciences, Keele University, ST5 5BG, UK*
[10]*European Southern Observatory, Karl-Schwarzschild-Str 2, D-85748 Garching bei München, Germany*
[11]*Institute of Astronomy, University of Cambridge, Madingley Road, Cambridge CB3 0HA, UK*

ABSTRACT

We present the results of the light curve model fitting technique applied to optical and near-infrared photometric data for a sample of 18 Classical Cepheids (11 fundamentals and 7 first overtones) in the Large Magellanic Cloud (LMC). We use optical photometry from the OGLE III data base and near-infrared photometry obtained by the European Southern Observatory public survey 'VISTA near-infrared survey of the Magellanic Clouds system'. Iso-periodic non-linear convective model sequences have been computed for each selected Cepheid in order to reproduce the multifilter light-curve amplitudes and shape details. The inferred individual distances provide an intrinsic weighted mean value for the LMC distance modulus of $\mu_0 = 18.56$ mag with a standard deviation of 0.13 mag. We derive also the Period–Radius, the Period–Luminosity, and the Period–Wesenheit relations that are consistent with similar relations in the literature. The intrinsic masses and luminosities of the best-fitting models show that all the investigated pulsators are brighter than the predictions of the canonical evolutionary mass–luminosity relation, suggesting a significant efficiency of non-canonical phenomena, such as overshooting, mass-loss, and/or rotation.

Key words: stars: oscillations – stars: variables: Cepheids – Magellanic Clouds – galaxies: structure.

1 INTRODUCTION

Classical Cepheids (CCs) are a class of pulsating stars widely used to calibrate the extragalactic distance scale, through secondary distance indicators. Their role as tool to measure distance is based on the relation they show between the period of pulsation and their intrinsic luminosity, known as period–luminosity (PL) relation. From an evolutionary point of view, a CC is a star with an intermediate mass (from 3 to 13 $M_\odot$), in the central helium burning phase (covering an age range from ∼10 to ∼200 Myr, see Anderson et al. 2017), that passes through the instability strip as

it evolves bluewards and then redwards (blue loop excursion), at roughly constant luminosity for each given mass. From a theoretical point of view, CCs, like all the other classes of pulsating stars, obey to a relation between the oscillation period and their mean density, as demonstrated by Eddington (1926). By combining this relation with the Stefan–Boltzmann law, one obtains a period–luminosity–mass–temperature relation. For CCs, this relation can be reduced to a period–luminosity–colour (PLC) relation because the theory of stellar evolution predicts the existence of a mass–luminosity relation (MLR), whose coefficients depend on the assumed metal and helium abundances. Currently adopted PL relation can be seen as a projection of the PLC relation on the PL plane (and references therein Freedman, Wilson & Madore 1991; Bono et al. 1999; Caputo et al. 2005). In other words, the PL relation shows an intrinsic dis-

* E-mail: roberto.molinaro@inaf.it

persion related to the finite width of the instability strip. Obviously, for each filter combination, both the PLC and its projection on the PL plane critically depend on the MLR. Since the efficiency of non-canonical phenomena (such as core overshooting, mass-loss, rotation) significantly affects the MLR, in order to determine precise distances using CCs, a detailed theoretical evaluation of the impact of these processes needs to be assessed.

Several authors have discussed the effect of mass-loss and core overshooting (see Chiosi, Wood & Capitanio 1993; Bono et al. 1999; Caputo et al. 2005; Keller & Wood 2006; Neilson et al. 2012; Marconi et al. 2013, and references therein), as well as of rotation (Anderson et al. 2016) on CC properties. These studies are often related to the so-called mass discrepancy problem, first outlined by Stobie (1969) and Christy (1970) and subsequently confirmed by additional investigations. According to these studies, the CC evolutionary mass (inferred from the comparison between theoretical isochrones and observations in the colour–magnitude diagram) was found to be systematically higher than the 'pulsational' one based on the period–mass–radius relation[1] (Fricke et al. 1972; Bono et al. 2001) or other methods based on the theory of pulsation (Bono, Castellani & Marconi 2002; Caputo et al. 2005). Keller & Wood (2006) and Marconi et al. (2013) adopted the model fitting of multifilter light, radial velocity, and radius curves to address the mass discrepancy. This is done through direct comparison of the observed and predicted variations along a pulsation cycle, the latter based on non-linear convective pulsational models (see Bono et al. 2000, 2002; Marconi et al. 2013, for a detailed discussion of the method).

The 'VISTA near-infrared Y, J, K_s survey of the Magellanic Clouds system' (VMC; Cioni et al. 2011) covers the Magellanic system with deep near-infrared (NIR) (Y, J, K_s filters) Tisserand (VIRCAM; Dalton et al. 2006) photometry using the ESO/VISTA telescope (Emerson, McPherson & Sutherland 2006). The main science goals of the VMC are the study of the spatially resolved star formation history (SFH) and the determination of the 3D structure of the whole Magellanic system. Particularly useful for the latter aim are pulsating variables such as RR Lyrae stars and CCs that have been the subject of several studies in the context of the VMC survey, as distance indicators and stellar population tracers (see e.g. Ripepi et al. 2012a,b, 2014, 2015, 2016, 2017; Moretti et al. 2014, 2016; Muraveva et al 2015, 2018).

Marconi et al. (2017) presented the model fitting of multiwavelength light curves and, when available, radial velocity curves of 12 Small Magellanic Cloud (SMC) CCs whose NIR observations were secured as part of the VMC data. The inferred stellar parameters and individual distances permitted to constrain not only the mean distance modulus of the SMC but also the behaviour of the investigated stars in the MLR, PL, period–radius (PR), and period–Wesenheit (PW) relations.[2]

---

[1]From the combination of the period–density relation and the Stefan–Boltzman law, it is also possible to obtain a period–mass–radius relation, which is useful to estimate the masses of Cepheids if their radii are known, and vice versa. According to the linear adiabatic theory, the pulsation period of variables is related to mass and radius through the equation $P = \alpha(M/M_\odot)^\beta(M/M_\odot)^\gamma$ (Fricke, Stobie & Strittmatter 1972), which can be linearized easily in logarithmic space ($\log P = \log \alpha + \beta \log (M/M_\odot) + \gamma \log (R/R_\odot)$) thus obtaining the Period-Mass-Radius (PMR) relation.

[2]The Wesenheit magnitudes include a colour term with a coefficient that corresponds to the ratio between total to selective extinction in the selected filter pair (Madore 1982; Caputo, Marconi & Musella 2000), thus making the Wesenheit relations reddening free.

In this paper, we extend this to a sample of 11 fundamental (F) and 7 first overtone (FO) CCs in the Large Magellanic Cloud (LMC), that are within the field of view of the VMC survey.

As regards the organization of the paper, in Section 2 we discuss the sample selection, in Section 3 we describe the adopted model fitting technique. The application of this technique to the selected LMC CCs and the implications of our results for the MLR, the PR, the PL, and PW relations are described in Sections 4 and 5, respectively. The final section includes a summary and perspectives.

2 SELECTION OF THE SAMPLE

The selected sample of CCs is composed of 11 and 7 F and FO pulsators, respectively, that cover a range in oscillation period from ∼1 to ∼30 d. The selected CCs have optical photometry from the OGLE III data base[3] (Soszyński et al. 2010) and NIR photometry from the VMC data base (see e.g. Cioni et al. 2011; Ripepi et al. 2016, 2017, for a description of VMC light curves). In particular, we used aperture photometry data from the Cambridge Astronomy Survey Unit (CASU) and the Vista Science Archive (see Cross et al. 2012; González-Fernández et al. 2018, for details). The sample is selected in order to span a wide range in period, luminosity, and shape of the light curves from the OGLE III data base. The period values spanned by our sample do not include the range of the so-called 'bump' Cepheids (8–12 d). However, this period range has already been analysed, using the same pulsating code as in this work, in Bono et al. (2002), where the authors selected a couple of LMC Cepheids, one with the bump on the rising branch and the other on the decreasing branch.

Although the number of the selected CCs does not represent the entire LMC, they let us test the prediction capabilities of the model fitting technique in a stellar system. We note that obtaining a statistically significant extension of the selected target number would be extremely time consuming to reach convergence of our hydrodynamical pulsation code.

The distribution in right ascension and declination of the selected CCs is shown in Fig. 1, where all known CCs in the LMC from the OGLE survey (Soszyński et al. 2015) are shown for comparison. The identification, the period, and the mean visual magnitude, of the selected CCs are listed in the first three columns of Table 1; these values were taken from Soszyński et al. (2015). As shown in Table 1, the selected CC sample encompasses wide ranges of periods and mean magnitude, thus allowing us to check the predictive capabilities of the model fitting technique over a large interval of CC observed properties.

3 THE MODEL FITTING TECHNIQUE

The fitting technique adopted to find the best model reproducing the observations, is similar to that described in Marconi et al. (2017):

(i) both observed and modelled photometric curves are phased in order to have the maximum of light at the same phase in a given reference band: e.g. in this work the maximum of light in the *V* band is at phase 0.

---

[3]When this work began OGLE IV data were not available. We checked for possible changes between the two data releases finding that the number of points in the *V* and *I* bands does not increase by more than a few per cents for most sources in our sample. Only for three stars the photometric observations increase significantly, but this does not affect the results of our method because a good phase coverage of light curves was already available in OGLE III.
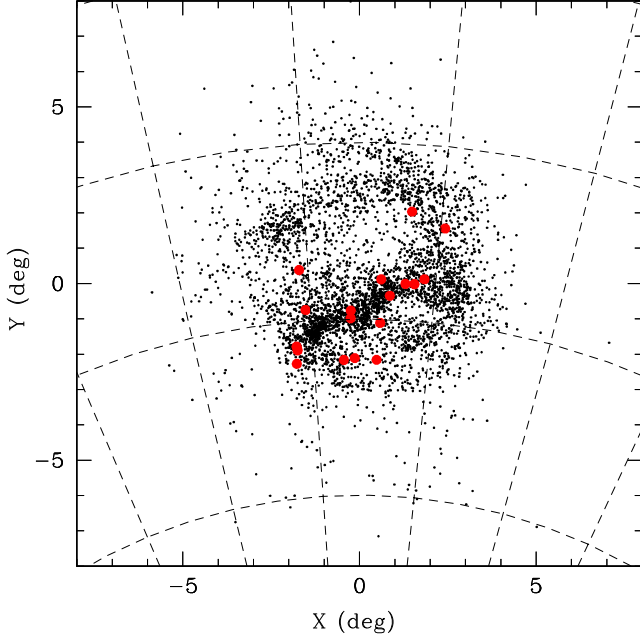
Figure 1. Distribution on the sky of the CCs investigated in this paper (the red filled circles). For comparison, the whole sample of known CCs in the LMC from the OGLE survey (the black dots) is shown. X and Y are defined as in van der Marel & Cioni (2001) with $\alpha_0 = 81°$ and $\delta_0 = -69°$.

(ii) for each modelled photometric band, we estimated the shifts in magnitude ($\delta\mu$) and phase ($\delta\phi$) that provide the best match between modelled and observed light curves. Specifically, these two parameters have been obtained by minimizing the following χ^2 equation:

$$\chi^2 = \frac{1}{N_{\text{bands}}} \sum_j^{N_{\text{bands}}} \frac{1}{N_{\text{DOF}}^j} \sum_i^{N_{\text{pts}}^j} \frac{[m_i^j - (M_{\text{mod}}^j(\phi_i^j + \delta\phi^j) + \delta\mu^j)]^2}{\sigma_i^j}, \quad (1)$$

where the two indices j and i run, respectively, on the number of bands, N_{bands}, and on the number of epochs, N_{pts}, the observed phases, magnitudes, and errors are indicated with ϕ_i^j and m_i^j, σ_i^j, respectively, while M^j is the absolute magnitude of the pulsating model evaluated at the same phase of observations plus the shift $\delta\phi$. To evaluate the model at a given phase, the theoretical light curves have been interpolated using a smooth spline. In the above formula, the term $N_{DOF}^j = N_{\text{pts}}^j - 2$ is the number of degrees of freedom for the jth band. We note that, because the initial phasing procedure, described above, is the same for observations and models, the fitted values of $\delta\phi$ are typically small (~ 0.02) and represent just fine-tuning phase shift values. On the other hand, the fitted parameter $\delta\mu^j$ represents the apparent distance modulus in the jth band.

Following the same approach as in Marconi et al. (2017), for each selected target CC, we built isoperiodic model sequences at fixed mass, varying the effective temperature and in turn the luminosity level. This allowed us to obtain a sample of light curve models with different shapes, magnitudes, and periods. Using this sample of models, we selected the model best matching the observed curves. The isoperiodic sequences are built using the typical elemental composition of the LMC ($Y = 0.25$; $Z = 0.008$; see Romaniello et al. 2008; Luck et al. 1998, for details). Once we found the best-fitting T_e, we built another sample of models varying the mass but fixing the obtained best-fitting temperature, again selecting the best-fitting model matching the observed curves. Thus, we were able to evaluate the mass, the luminosity, the effective temperature of the star, and in turn its individual apparent distance modulus in each selected band.

In Fig. 2, we show an example of the model fitting dependence on the assumed effective temperature (fixed mass $M = 4.0 \, M_\odot$) and stellar mass (fixed $T_{\text{eff}} = 6175$ K). The χ^2 analysis for models with fixed mass identifies as best-fitting effective temperature $T_{\text{eff}} = 6175$ K, as shown in the top panel of the quoted figure. Then varying the mass (Fig. 2 bottom panels), one obtains the best-fitting value $M = 3.8 \, M_\odot$. Since it is difficult to evaluate by eye the quality of the fit shown in Fig. 2, in Fig. 3 we show the total reduced χ^2 as a function of the model effective temperature (top) and mass (bottom).
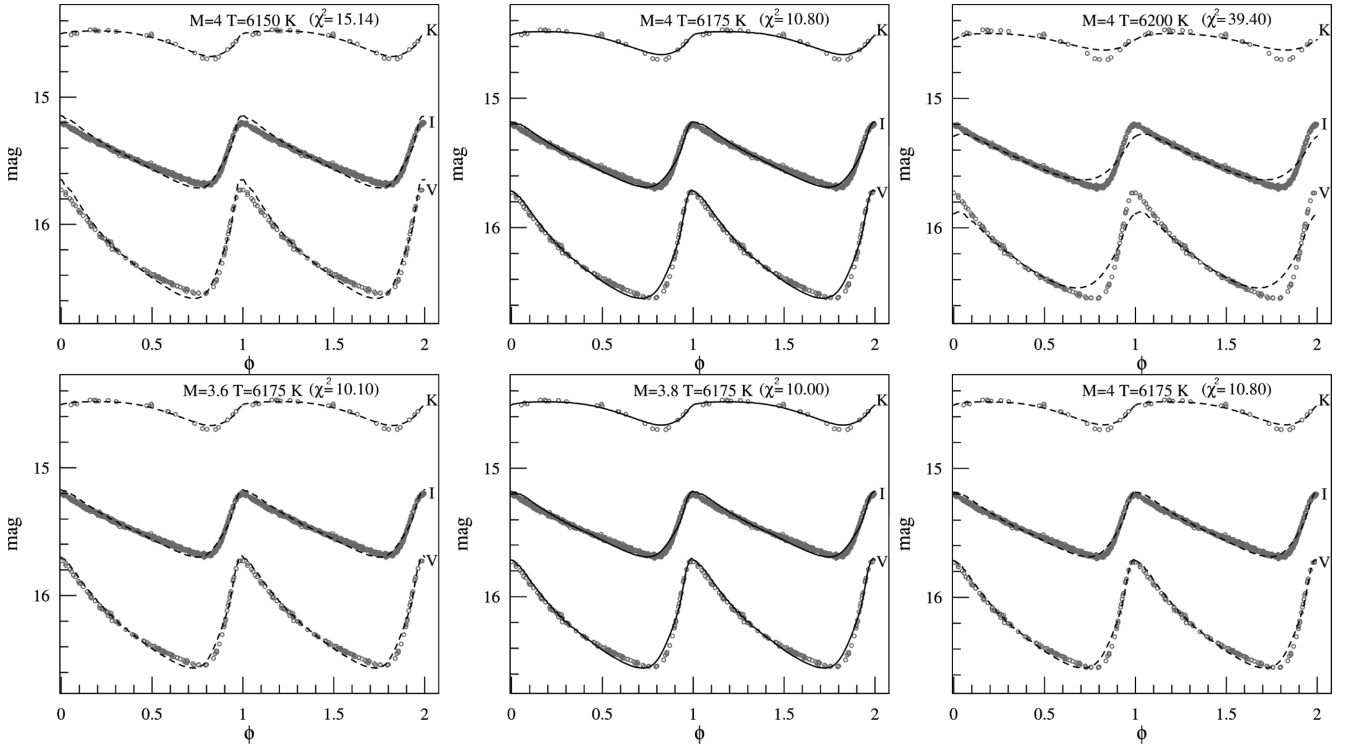
Table 1. Properties of the target CCs and of the associated best-fitting models. From left to right: OGLE identification, observed period, mean V magnitude, and pulsation mode (from the OGLE III data base Soszyński et al. 2010), best-fitting model mass, luminosity, effective temperature, mixing length parameter, inferred distance modulus in the V, I, and K_s bands and associated errors, absolute distance modulus with associated error, magnitude correction to refer distance modulus to LMC barycentre, reddening with associated error, mean radius, and χ^2 value. For all CCs, the error in the inferred mass and temperature is $\Delta T = 25$ K and $\Delta M = 0.2 \, M_\odot$, respectively; the assumed composition is $Y = 0.25$, $Z = 0.008$, except for $OGLE\_LMC\_CEP\_2019$ for which $Y = 0.30$ (see text).

ID	P (d)	$\langle V \rangle$ (mag)	Mode	M ($M_\odot$)	$\log(L/L_\odot)$ (dex)	T_{eff} (K)	α_{ML}	μ_V (mag)	μ_I (mag)	μ_K (mag)	μ_0 (mag)	μ_0^{corr} (mag)	$E(B-V)$ (mag)	R ($R_\odot$)	χ^2
1481	0.922	17.28	FO	3.00	2.62	6650	1.50	19.14 ± 0.10	18.89 ± 0.07	18.49 ± 0.08	18.42 ± 0.09	0.002	0.24 ± 0.05	15.4	0.9
3131	1.095	17.01	FO	2.80	2.63	6450	1.80	18.89 ± 0.05	18.72 ± 0.03	18.52 ± 0.02	18.47 ± 0.02	0.02	0.14 ± 0.01	16.6	1.0
3004	1.524	17.15	F	3.00	2.65	6425	1.60	19.08 ± 0.08	18.86 ± 0.04	18.55 ± 0.01	18.48 ± 0.01	-0.04	0.19 ± 0.03	17.2	6.0
1523	1.572	16.88	F	2.80	2.64	6425	1.60	18.78 ± 0.08	18.62 ± 0.04	18.44 ± 0.02	18.39 ± 0.02	0.05	0.13 ± 0.02	17.0	3.4
3113	2.068	16.08	FO	5.20	3.15	6300	1.60	19.27 ± 0.05	19.06 ± 0.03	18.77 ± 0.01	18.71 ± 0.01	0.008	0.18 ± 0.02	31.5	1.2
2138	3.011	16.21	F	3.80	3.03	6175	1.70	19.04 ± 0.07	18.85 ± 0.05	18.60 ± 0.05	18.54 ± 0.05	0.04	0.16 ± 0.02	28.7	10.0
3105	3.514	15.38	FO	4.80	3.33	6050	1.60	18.96 ± 0.06	18.82 ± 0.04	18.62 ± 0.03	18.58 ± 0.03	0.011	0.13 ± 0.01	42.2	1.0
0961	3.711	15.87	F	3.90	3.11	6100	1.70	18.90 ± 0.07	18.76 ± 0.06	18.54 ± 0.07	18.49 ± 0.07	0.018	0.13 ± 0.02	32.5	7.4
1475	4.387	15.19	FO	5.60	3.48	5985	1.51	19.14 ± 0.09	19.01 ± 0.08	18.77 ± 0.06	18.73 ± 0.06	0.03	0.13 ± 0.01	51.2	3.2
1124	4.457	15.81	F	5.00	3.29	6040	1.70	19.24 ± 0.08	19.06 ± 0.06	18.79 ± 0.03	18.73 ± 0.03	0.014	0.16 ± 0.02	40.5	13.4
1310	5.126	17.28	FO	5.70	3.54	5950	1.49	18.78 ± 0.04	18.71 ± 0.05	18.60 ± 0.05	18.58 ± 0.06	0.015	0.07 ± 0.01	55.5	2.6
0813	5.914	14.54	FO	7.00	3.66	5850	1.53	18.93 ± 0.07	18.87 ± 0.05	18.75 ± 0.03	18.73 ± 0.03	0.02	0.07 ± 0.01	66.2	4.2
2012	7.458	14.95	F	6.50	3.54	5775	1.90	18.98 ± 0.03	18.88 ± 0.02	18.71 ± 0.01	18.68 ± 0.01	0.008	0.10 ± 0.01	59.4	7.0
1954	12.950	14.61	F	5.30	3.69	5575	1.90	19.00 ± 0.07	18.81 ± 0.05	18.61 ± 0.02	18.55 ± 0.02	0.04	0.14 ± 0.02	75.8	13.4
0546	15.215	14.03	F	5.20	3.77	5575	1.70	18.59 ± 0.11	18.58 ± 0.11	18.57 ± 0.10	18.56 ± 0.11	-0.003	0.01 ± 0.02	83.9	44.2
1086	17.201	14.35	F	5.40	3.75	5350	1.90	18.86 ± 0.09	18.76 ± 0.08	18.64 ± 0.08	18.61 ± 0.08	-0.03	0.08 ± 0.02	89.5	17.7
2944	20.320	14.30	F	6.90	3.95	5400	1.84	19.30 ± 0.06	19.15 ± 0.06	18.83 ± 0.07	18.78 ± 0.08	-0.010	0.17 ± 0.02	108.6	9.3
2019	28.103	13.64	F	7.70	4.11	5425	1.70	19.00 ± 0.07	18.83 ± 0.06	18.67 ± 0.04	18.62 ± 0.05	0.013	0.12 ± 0.02	131.9	5.3

Figure 2. Comparison of the observed *V*, *I*, and *K_s* light curves of the variable OGLE LMC CEP 2138 and the fitted theoretical light curves. Data are plotted with the grey symbols, while models are plotted with the lines. In the top panels, we show the models calculated assuming a fixed mass, namely ($M = 4.0\,\mathrm{M_\odot}$) and varying effective temperature. Once the model with best T_e (namely $T_e = 6175$ K) is found (the solid line), the effective temperature is maintained fixed at its best value and the χ^2 in equation (1) is minimized by varying the mass. Models with varying mass and fixed T_e are showed in the bottom panels, where the final best-fitting model is again indicated with a solid line and is characterized by $T_e = 6175$K and $M = 3.8\,\mathrm{M_\odot}$. The χ^2 values of the fit are also labelled in each panel.

Looking at the best χ^2 value in the figure and also at those reported in the Table 1, it is evident that they are not always close to the expected canonical value $\chi^2 = 1$. This is due both to error underestimation of the observations and to the difficulty to reproduce exactly light curves with more complex shapes (see also Fig. 5). The presence of features in the light curves of pulsating variables, which make them more complex from the shape point of view, is due to the coupling between pulsation and convection that becomes more important moving towards the red boundary of the instability strip (see Bono, Marconi & Stellingwerf 1999, and references therein). On this basis, we expect a correlation between the χ^2 values and the best-fitting effective temperature in the sense that lower χ^2 values correspond to higher effective temperatures. This trend is evident in Fig. 4 where the χ^2 values of Table 1 are plotted against the best-fitting effective temperature T_e,[4] with lager χ^2 values populating the zone of lower effective temperaures. Moreover, a clear separation can be seen between F and FO models, the latter having smaller χ^2 values and as well as known higher effective temperatures.

4 APPLICATION TO THE SELECTED VARIABLES

The procedure detailed in the previous section was applied to all CCs in Table 1 and the corresponding models are shown in Fig. 5.

[4]Note that the source OGLE_LMC_CEP_0546 does not appear in Fig. 4 because of its χ^2 value is out of the *y*-axis range.

We note that for the longest period CC in our sample (namely $OGLE\_LMC\_CEP\_2019$) we had to vary also the elemental composition in order to reproduce the observed light curves. For this star, we adopted $Y = 0.30$, $Z = 0.008$. The inferred intrinsic stellar parameters, namely the effective temperature, the luminosity, and the mass of the best-fitting models are reported in Table 1 with their errors.

In particular, the errors on the parameters obtained from the fitting procedure are estimated as the difference between the best values and the parameters of the closest models to the best-fitting one on the mass–temperature grid. As regard the error on the mass and temperature of the best model, we have adopted the steps of the mass–temperature model grid (0.2 $\mathrm{M_\odot}$ and 25 K, respectively) generated for our analysis.

The quoted table contains also the unreddened distance moduli μ_0 and the $E(B - V)$ values for all stars considered in this work. They have been calculated by fitting the Cardelli law (Cardelli, Clayton & Mathis 1989) to the inferred apparent distance moduli in the *V*, *I*, *K_s* bands.

A simple statistical analysis of the values reported in Table 1 gives a mean value of the reddening equal to $E(B - V) = 0.13$ mag with a standard deviation of 0.05 mag, while the inferred mean distance modulus for the LMC is equal to $\mu_0 = 18.59$ mag with a standard deviation equal to 0.12 mag. Weighting the fitted parameters with their errors provides almost the same values, with mean distance modulus that is equal to $\mu_0^{wt} = 18.63$ mag ($\sigma^{wt} = 0.10$ mag) and the mean reddening $E(B - V)^{wt} = 0.11$ mag ($\sigma^{wt} = 0.04$ mag).

In order to take into account the effect of the inclination of the plane of the LMC with respect to the sky on the barycentric
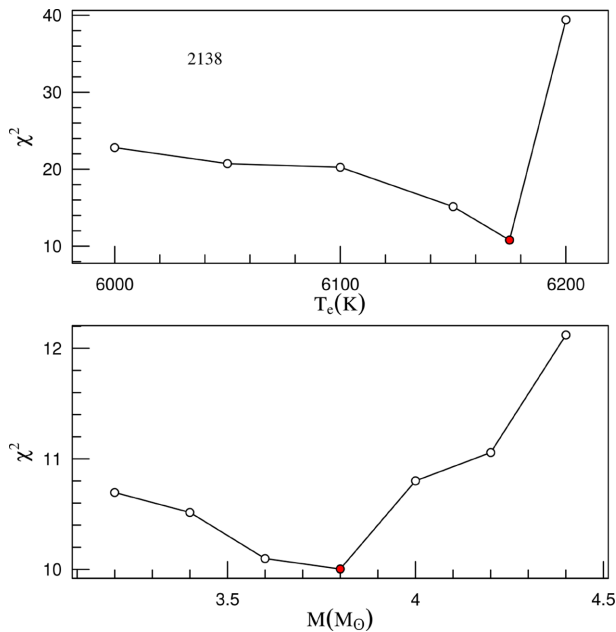
Figure 3. Total reduced χ^2 values obtained from the fitting procedure applied to $OGLE_LMC_CEP_$2138 are shown as a function of the model effective temperature (top) and mass (bottom). The values of the best effective temperature and mass are indicated by the red dots.
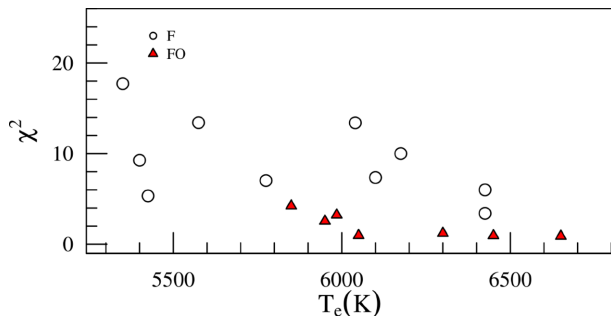

Figure 4. The χ^2 values obtained from the fitting procedure and listed in Table 1 are plotted against the best values of effective temperature for all sources of the selected sample: F pulsators are shown using the empty circles, while FOs are plotted with the red triangles.

distance estimation, we have also calculated the magnitude corrections (see Table 1) for every CC of our sample according to the geometric model by van der Marel & Cioni (2001). A statistical analysis of the distances obtained by including the quoted corrections does not change the results reported above about the LMC distance.

As stated in the previous section, the χ^2 values exhibit a large scatter (see Table 1) indicating that the more complex light curve shapes are modelled with lower accuracy and larger residuals. Therefore, we decided also to weigh the best parameters using the χ^2 values to define the weights (wts $= 1/\chi^2$) in order to favour those models that better describe the observed light curve shapes. The resulting weighted distance modulus is equal to $\mu_0^{\mathrm{wt}_{\chi^2}} = 18.56$ mag with a standard deviation $\sigma^{\mathrm{wt}_{\chi^2}} = 0.13$ mag. We assume that this value is our best estimate of the LMC distance. Using the same χ^2-weighted statistics for the excess, we obtain a mean value equal to $E(B-V)^{\mathrm{wt}_{\chi^2}} = 0.15$ mag with a standard deviation equal to $\sigma^{\mathrm{wt}_{\chi^2}} = 0.05$ mag.

The quoted errors represent only the statistical uncertainties, while the systematic is difficult to estimate but depends on the physical and numerical assumptions of the current model sets as well as on residual uncertainties of the adopted atmosphere models. Moreover, the above results for the distance modulus do not take into account projection effects, related to the fact that CCs are not located at the centre of the LMC.

5 RESULTS

In this section, we use the results obtained for the intrinsic stellar parameters of the investigated CCs to determine constraints both on the predicted MLR and PR relations as well as on the PL and PW relations, at least for the assumed elemental composition.

5.1 The mass–luminosity relation

Fig. 6 displays the MLR for the investigated CCs whose intrinsic stellar parameters were derived from the best-fitting models listed in Table 1. These data are compared with the predicted canonical (no overshooting, no mass-loss) MLR (Bono et al. 2000; the solid lines) and with the relations obtained by increasing the zero-point of the canonical MLR by 0.25 dex (the dashed lines) and 0.5 dex (the dotted lines) to reproduce the effect of mild and full overshooting,[5] respectively (see Chiosi et al. 1993; Bono et al. 1999, for details). Inclusion of mass-loss and/or rotation would produce a similar increase in the Cepheid luminosity level at fixed mass (see Neilson et al. 2012, for details). As the light curves of $OGLE_CEP_LMC_$2019 are best reproduced adopting a different value of the helium content (see above), in Fig. 6 we also show the MLR for $Y = 0.30$, $Z = 0.008$ (the green lines). Note that this relation is slightly more luminous than those calculated for the standard LMC elemental composition ($Y = 0.25$, $Z = 0.008$). According to the location of the variables in the ML plane, the canonical MLR is not strictly satisfied, as the points are spread between the canonical and full overshooting predictions. Even if at this stage we cannot disentangle the role of overshooting, mass-loss, and rotation in producing the quoted excess luminosity, at fixed mass, the detected dispersion might indicate a combination of these different non-canonical phenomena. Indeed, if only overshooting were efficient, one would in principle expect the same amount of excess luminosity for all stellar masses (within small uncertainties). Rotation produces similar effects as overshooting because it implies a larger He burning core and a brighter luminosity at fixed mass (see e.g. Anderson et al. 2016) On the other hand, if the mass-loss process were efficient, this could be inferred from the predicted deviation of the best-fitting stellar mass from the value corresponding to the canonical MLR. Such a deviation is represented in Fig. 7 as a function of the canonical mass (top) and of the pulsation period (bottom) for the CCs in our sample. We note that the expected mass differences range from 0 per cent to almost ~ 50 per cent and are not clearly correlated with the pulsation period or the stellar mass.

5.2 The period–mass–radius and the period–radius relations

Once we obtain the mass and the radius from the output of the non-linear hydrodynamical code, we are able to correlate them with

---

[5]Corresponding to an extension of the extramixing region beyond the Schwarzschild border of about $0.2H_{\mathrm{p}}$, where H_{p} is the pressure scale height (Chiosi et al. 1993).
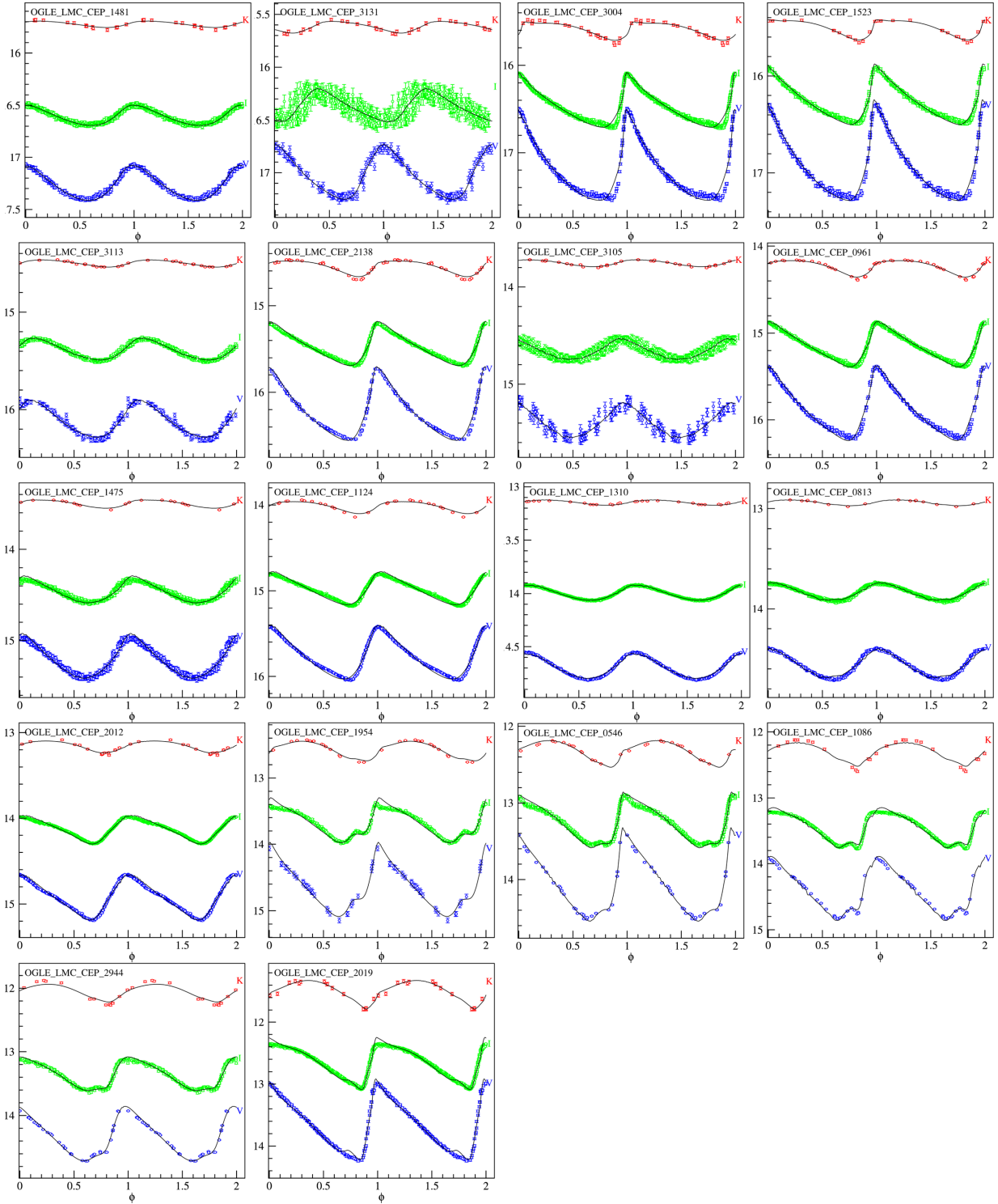
Figure 5. Best-fitting models for all selected CCs compared with the observed light curves. The black lines represent the theoretical models, while the *V*, *I*, and *K_s* observed light curves are labelled together with star identifications.

the pulsational period for each CC to investigate the PMR relation. Assuming the linearized equation introduced above, we obtain

$$\log P = (-1.618 \pm 0.007) + (-0.68 \pm 0.02) \log(M/M_\odot)$$
$$+ (1.72 \pm 0.01) \log(R/R_\odot) \tag{2}$$

with a $\sigma = 0.005$ dex. The values of the fitted parameters are in excellent agreement with those expected from linear theory (see e.g. Fricke et al. 1972).

If we neglect the mass dependence in the PMR relation, we can obtain the PR relation, which is also well studied in the literature (see e.g. Gieren, Moffett & Varnes 1999; Molinaro et al. 2011, 2012, and references therein). The location of the 18 investigated CCs in
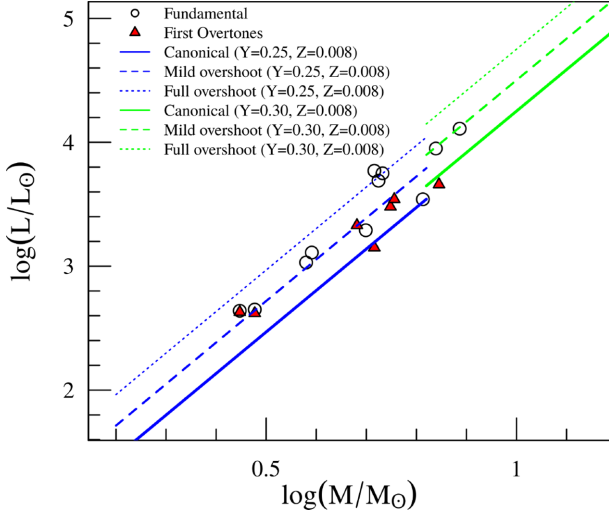
Figure 6. Predicted MLR based on the model fitting results for both F (the empty circles) and FO CCs (the red filled triangles). The best-fitting model location in the MLR plane is compared with an evolutionary MLR obtained by neglecting mass-loss, core overshooting, and rotation (labelled 'Canonical') and with the relations obtained by assuming mild or full overshooting (see text for detail).
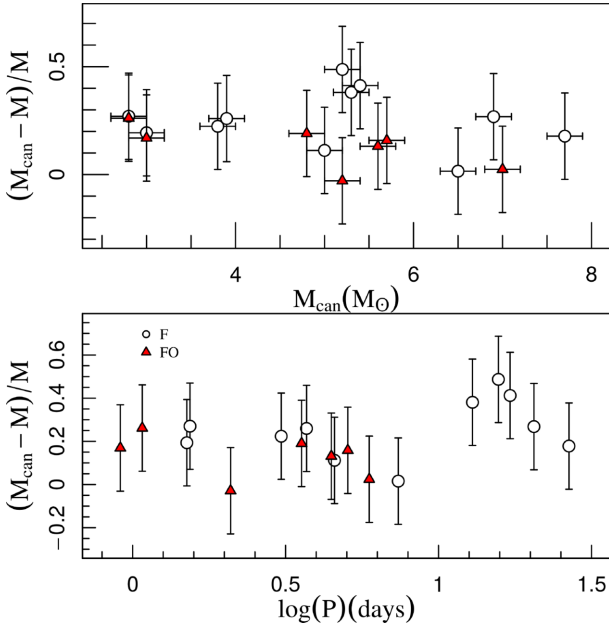

Figure 7. Deviation of the best-fitting stellar mass from the value corresponding to the canonical mass for both F (the empty circles) and FO (the red triangles) CCs.

the (PR) diagram is shown in Fig. 8, where Fs are plotted using empty circles and FOs with the filled triangles; the periods of the FO pulsators have been fundamentalized using the equation given by Feast & Catchpole (1997). A linear regression fit to the data gives us the following PR relation:

$$\log(R/R_\odot) = (0.70 \pm 0.02) \log(P) + (1.12 \pm 0.01), \quad (3)$$

which is displayed with a black line in Fig. 8 with a $\sigma = 0.03$ dex. The same figure shows, for comparison, the PR relations of Molinaro et al. (2012; the red line) and Gieren et al. (1999; the blue
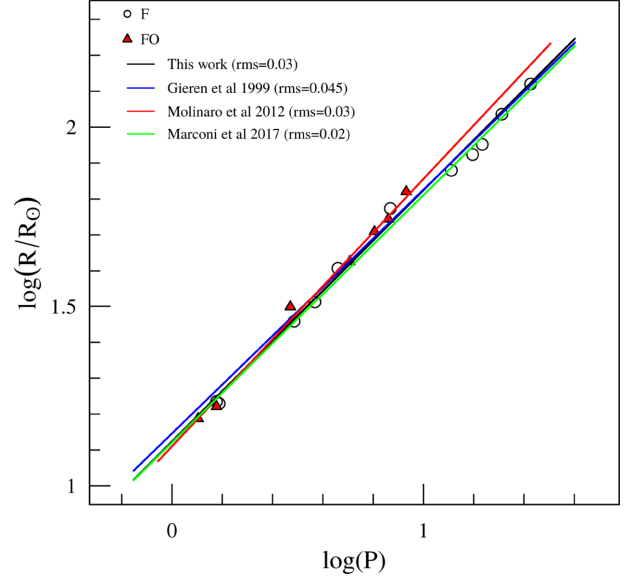

Figure 8. The Cepheid PR relation obtained for the selected sample of 18 sources. The CCs are plotted using the empty circles and the filled triangles, respectively for Fs and FOs; the FO periods have been fundamentalized (see text). The black line is the result of a linear regression fit to the data (see text). For comparison the PR relations of Gieren et al. (1999; the blue line), Molinaro et al. (2012; the red ine) and Marconi et al. (2017; the green line) are also plotted.

line), based on two different realizations of the Baade–Wesselink method, and the relation of Marconi et al. (2017; the green line), which was obtained using the model fitting technique for a sample of CCs in the SMC. The PR relation of Molinaro et al. (2012) is based on a sample of 11 CCs belonging to the young LMC blue populous cluster NGC 1866 and 26 Galactic CCs (see also Molinaro et al. 2011), while the PR relation of Gieren et al. (1999) has been derived from a sample of both Galactic and Magellanic CCs. Inspection of Fig. 8 and a comparison of the coefficients of the plotted relations reveal that the PR found in this work is in agreement with those of Gieren et al. (1999) and Molinaro et al. (2012). In particular, the result of Gieren et al. (1999) predicts a shallower relation but it is in excellent agreement (1σ) with our PR, while the slope of Molinaro et al. (2012) is steeper than that obtained in this work, though it is consistent within $\sim 2\sigma$. Concerning the intercepts of relations, they are in excellent agreement (1σ) with that found in this work. The Baade–Wesselink technique is known to be dependent on the adopted value of the projection factor (p-factor), which allows to convert spectroscopically measured radial velocity into pulsational velocity (see Gieren et al. 1999; Molinaro et al. 2011, 2012; Gallenne et al. 2017; Kervella et al. 2017; Nardetto et al. 2017, and their references for a discussion). Since the radii obtained from pulsating models are not dependent on this key parameter, comparing the results from the two techniques allows us to put constraints on the p-factor. As for the cases discussed in this work, Molinaro et al. (2012) adopted a constant p-factor of 1.27, while Gieren et al. (1999) used a period dependent value ($p = 1.39 - 0.03 \log P$) from Hindsley & Bell (1986). Since both results are consistent with the PR obtained from pulsational models, we are not able to single out one of the two choices as better.

In order to compare the PR relations by Gieren et al. and Molinaro et al., using the same projection factor, we rescaled first the results from the former work to the constant p-factor value adopted by
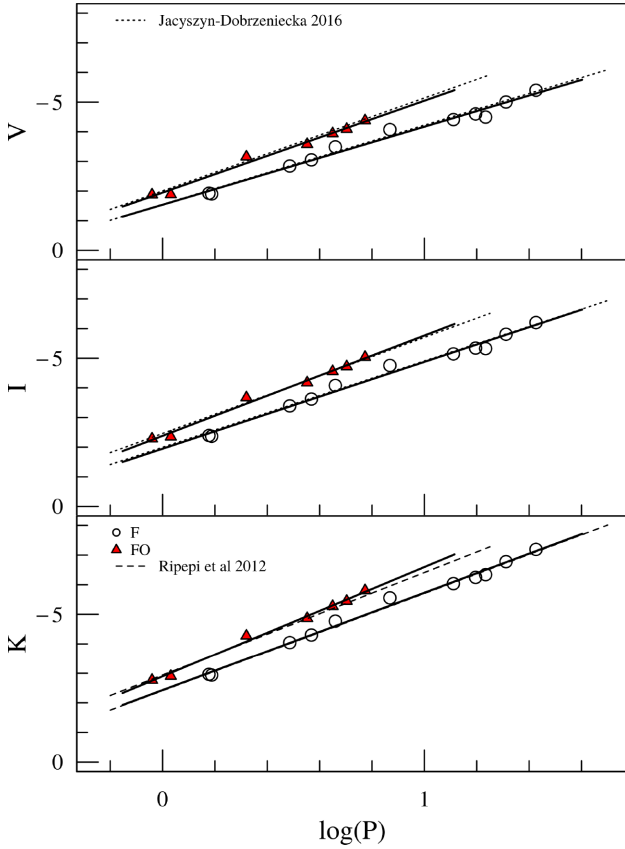
Figure 9. Predicted PL relation in the *V* (top), *I* (middle), and K_s (bottom) bands based on the model fitting results for both F (the empty circles) and FO (the red filled triangles) CCs. The three panels show also PL relations from the literature obtained, namely, by Ripepi et al. (2012b) in the K_s band (the dashed line) and by Jacyszyn-Dobrzeniecka et al. (2016) in the *V* and the *I* bands (the dotted lines).

Molinaro et al., and then the results from the latter work to the variable p-factor used by Gieren et al. From this procedure, we can conclude that the best agreement with the PR relation in equation (3) is obtained using the visual surface brightness technique from Gieren et al., but adopting a constant p-factor as in Molinaro et al. In particular, in the quoted case we obtain the fitted PR relation $\log(R/R_\odot) = (0.699 \pm 0.017)\log P + (1.11 \pm 0.02)$, which is almost the same as that of equation (3).

We also compare our PR relation with that of Marconi et al. (2017), obtained for a sample of SMC CCs using the model fitting technique. Their fitted relation is given by $\log(R/R_\odot) = (0.690 \pm 0.017)\log P + (1.121 \pm 0.016)$ and is fully consistent with our result, indicating that samples with different elemental compositions obey the same PR relation, in agreement with the theoretical results obtained by Bono, Caputo & Marconi (1998).

5.3 The PL Relation

The mean absolute magnitudes of the best-fitting models can be correlated with the corresponding periods to build multifilter PL relations. In Fig. 9, we show the location of both F (the empty circles) and FO (the red filled triangles) best-fitting models in the *V*, *I*, and K_s bands versus period. In each panel, the solid line shows the linear regression fit to the data points whose coefficients are listed in Table 2. To compare our theoretical relations with

Table 2. Coefficients of the inferred period–radius, period–luminosity, and period–Wesenheit relations (in the *V*, *I*, K_s bands), respectively. Columns 4–8 represent the slope (α) and the intecept (β) with their associated errors (σ_α, σ_β), and the rms of the residuals around the fitted relation.

	Mode	Band	α	σ_α	β	σ_β	rms
PR			0.70	0.02	1.12	0.01	0.03
PL	F	*V*	−2.63	0.11	−1.54	0.11	0.16
	FO		−3.10	0.16	−1.95	0.09	0.13
	F	*I*	−2.93	0.11	−1.95	0.10	0.15
	FO		−3.38	0.15	−2.38	0.08	0.12
	F	K_s	−3.30	0.09	−2.43	0.09	0.13
	FO		−3.70	0.14	−2.90	0.07	0.11
PW	F	$W(V, I)$	−3.39	0.10	−2.58	0.09	0.14
	FO		−3.83	0.13	−3.06	0.07	0.11
	F	$W(V, K_s)$	−3.39	0.09	−2.55	0.09	0.13
	FO		−3.78	0.13	−3.02	0.07	0.11

those obtained by other authors, we have also plotted in the three panels the PL of Jacyszyn-Dobrzeniecka et al. (2016), in the *V* and *I* bands, and of Ripepi et al. (2012b) for the K_s band. Since the relations given by Jacyszyn-Dobrzeniecka et al. (2016) contain apparent magnitudes, we have first corrected them for absorption using the mean $E(B − V)$ value obtained in this work, and then shifted them using our best estimate of the LMC distance modulus. The comparison of the slope values provided by these authors ($\alpha_V^F = -2.672 \pm 0.006$, $\alpha_V^{FO} = -3.133 \pm 0.006$, $\alpha_I^F = -2.911 \pm 0.006$, and $\alpha_I^{FO} = -3.240 \pm 0.006$) shows an excellent agreement in the *V* band. For the *I* band, the two slopes are different, but still consistent because of our large error. The K_s band PL relations for Fs and FOs of Ripepi et al. (2012b) contain absolute magnitudes and consequently can be directly compared with our results in the corresponding band. From this comparison, we found that the coefficients of their relation ($\alpha_K^F = -3.295 \pm 0.018$, $\beta_K^F = -2.41 \pm 0.03$) are in excellent agreement with our results for F pulsators. As for the FO mode, their zero-point ($\beta_K^F = -2.94 \pm 0.07$) is in excellent agreement with our value, while their slope ($\alpha_K^F = -3.471 \pm 0.035$) is consistent with our result within ~1.5σ.

Inspection of the results in Table 2 also suggests that the derived rms of residuals around the PL relations are of the same order of magnitude as that obtained for the observational relations (Ripepi et al. 2012b; Jacyszyn-Dobrzeniecka et al. 2016).

5.4 The Wesenheit relation

Finally, it is interesting to compare the PW relations found in this work with those adopted in the literature (e.g Ripepi et al. 2012b; Jacyszyn-Dobrzeniecka et al. 2016). To estimate the Wesenheit magnitudes for the optical and NIR data, we use the following definitions: $W(V, I) = I - 1.55 \times (V - I)$ and $W(V, K_s) = K_s - 0.13 \times (V - K_s)$, according to recent prescriptions in the literature (see e.g. Soszyński et al. 2015; Ripepi et al. 2016, and references therein). The PW relations for the investigated CCs are shown in Fig. 10, where the symbols have the same meaning as in Fig. 9. The bottom panel shows the relation obtained by combining optical and NIR bands, and the top panel shows the same relation obtained using only optical bands. The linear regression fits to the data are also shown (the solid lines) and the coefficients are reported in Table 2.

The PW equations in the optical bands are provided by Jacyszyn-Dobrzeniecka et al. (2016) and are based on apparent magnitudes.
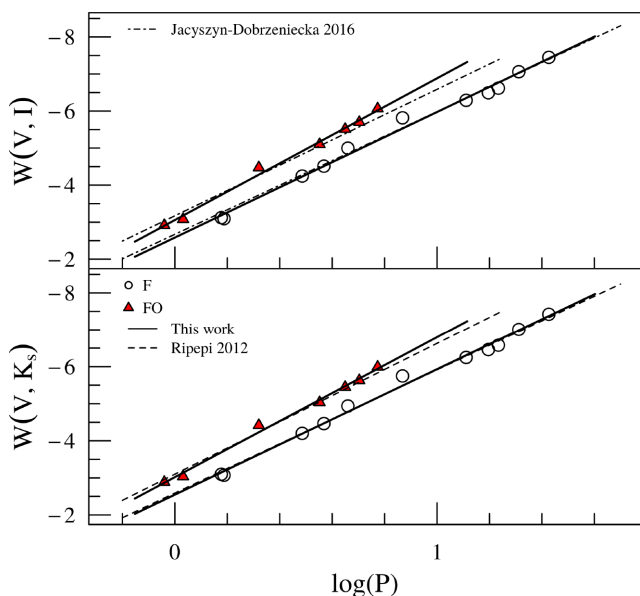
Figure 10. Predicted PW relations in the V, I (top) and V, K_s (bottom) filters for both F and FO pulsators. Symbols are as in the Fig. 9. For comparison with literature results, in the top panel we show also the relation of Jacyszyn-Dobrzeniecka et al. (2016; the dot–dashed lines), while in the bottom panel we plot the relations of Ripepi et al. (2012b; the dashed lines).

In order to compare them with the results obtained in this work, we have shifted their F and FO relations using our best estimate of the LMC distance modulus $\mu = 18.56$ mag. Looking at the top panel of Fig. 10, we note that the relations for F Cepheids are in excellent agreement, being almost coincident, while the theoretical FO PW relation seems to be steeper than the relation by Jacyszyn-Dobrzeniecka et al. (2016). Indeed, their slope $\alpha_{W(V,I)}^{FO} = -3.414 \pm 0.007$ differs from our estimate by more than 3σ.

The $W(V, K_s)$ relations provided by Ripepi et al. (2012b) are expressed using absolute magnitudes and consequently can be directly compared with our results. Their equation for F pulsators ($W(V, K_s) = (-3.325 \pm 0.014)\log P + (-2.59 \pm 0.03)$) is in excellent agreement with our result (see Table 2), with both slope and intercept being consistent within less than 1σ. The coefficients of their FO equation ($W(V, K_s) = (-3.530 \pm 0.025)\log P + (-3.10 \pm 0.07)$), are consistent with our estimates within $\sim 1.5\sigma$.

6 CONCLUSIONS

We considered a sample of 11 F and 7 FO CCs in the LMC with optical photometry from the OGLE III data base and NIR photometry from the VMC survey. By assuming first approximation elemental composition typical of LMC CCs ($Y = 0.25$, $Z = 0.008$), for each selected pulsator, we built isoperiodic model sequences varying the intrinsic stellar properties (effective temperature, mass/luminosity) in order to match the period, and the shape of the observed light curves in the V, I, and K_s bands. The resulting models directly provide information on the mass, the effective temperature, the luminosity, and in turn the individual distance of each selected target VMC CC. On this basis, we obtained the following results:

(i) From the inferred apparent distance moduli, adopting the extinction law by Cardelli et al. (1989) we obtained an estimate

of the intrinsic distance modulus for every star in our sample. We decided to weigh these values using the best-fitting χ^2 to give and an estimate of the LMC distance modulus. Our procedure provides a value of $\mu_0 = 18.56$ mag with a standard deviation of 0.13 mag, in agreement with the most recent literature values (Marconi & Clementini 2005; Marengo et al. 2010; Ripepi et al. 2012a; Pietrzyński et al. 2013; de Grijs, Wicker & Bono 2014; Jacyszyn-Dobrzeniecka et al. 2016). We note that our best value for the LMC distance modulus is in perfect agreement with the results of one of our previous applications (18.53 ± 0.05 mag Bono et al. 2002) and the estimate by Keller & Wood (2006), 18.54 ± 0.018 mag, obtained using a similar approach for a sample of bump Cepheids covering a pulsation period range centred on 10 d, an almost complementary range compared to the sample analysed in this work.

(ii) Considering the geometric correction according to the model by van der Marel & Cioni (2001) in the estimation of the LMC distance has no effect on the quoted results.

(iii) the MLR is clearly more luminous than the evolutionary MLR that neglects overshooting, mass-loss, and rotation, thus suggesting a high efficiency of at least one of these non-canonical phenomena.

(iv) A PR relation in agreement with the literature results, in particular with the relation of Gieren et al. (1999).

(v) Theoretical PL relations in the V, I, and K_s bands adequately reproduce the observed intrinsic scatter of the PL distribution.

(vi) Theoretical PW relations are in agreement with the empirical LMC Wesenheit relations recently presented by Ripepi et al. (2012b).

We note that for one long-period Cepheid we needed to vary the elemental composition in order to obtain a satisfactory fit. In particular for CC $OGLE\_CEP\_LMC\_2019$ an enhanced helium abundance $Y = 0.30$ was required in order to fit the observed curve. The possible presence of a fraction of helium enriched CCs has been recently theoretically investigated by Carini et al. (2017), following previous indications of the presence of multiple stellar populations in young LMC star clusters (see e.g. Milone et al. 2016, and references therein).

In the future, we also plan to extend the application to other samples of pulsators in order to better constrain their PL and PW relations and to test the accuracy of the method through application to the light curves of Galactic CCs with *Gaia* parallaxes (Gaia Collaboration 2018). The latter comparison, once we have fixed the distance to the *Gaia* results, will also allow us to put strong constraints on the predicted stellar masses, the MLR, and, once the metallicity is precisely constrained by complementary spectroscopic data, the helium to metal enrichment ratio.

REFERENCES

Anderson R. I., Saio H., Ekström S., Georgy C., Meynet G., 2016, A&A, 591, A8

Anderson R. I., Ekström S., Georgy C., Meynet G., Saio H., 2017, in Catelan M., Gieren W., eds, EPJ Web of Conf. 152, Wide Field Variability Surveys: A 21st Century Perspective 22nd Los Alamos Stellar Pulsation. San Pedro de Atacama, Chile, p. 06002

Bono G., Caputo F., Marconi M., 1998, ApJ, 497, L43

Bono G., Caputo F., Castellani V., Marconi M., 1999, ApJ, 512, 711

Bono G., Marconi M., Stellingwerf R. F., 1999, ApJS, 122, 167

Bono G., Caputo F., Cassisi S., Marconi M., Piersanti L., Amedeo T., 2000, ApJ, 543, 955

Bono G., Gieren W. P., Marconi M., Fouqué P., Caputo F., 2001, ApJ, 563, 319

Bono G., Castellani V., Marconi M., 2002, ApJ, 565, L83

Caputo F., Marconi M., Musella I., 2000, A&A, 354, 610

Caputo F., Bono G., Fiorentino G., Marconi M., Musella I., 2005, ApJ, 629, 1021

Cardelli J. A., Clayton G. C., Mathis J. S., 1989, ApJ, 135, 5

Carini R., Brocato E., Raimondo G., Marconi M., 2017, MNRAS, 469, 1532

Chiosi C., Wood P. R., Capitanio N., 1993, ApJS, 86, 541

Christy R. F., 1970, J. R. Astron. Soc. Can., 64, 8

Cioni M.-R. L. et al., 2011, A&A, 527, A116

Cross N. J. G. et al., 2012, A&A, 548, A119

Dalton G. B. et al., 2006, in McLean I. S., Masanori I., eds, Proc. SPIE Conf. Ser. Vol. 6269, Ground-based and Airborne Instrumentation for Astronomy. SPIE, Bellingham, p. 62690X

de Grijs R., Wicker J. E., Bono G., 2014, AJ, 147, 122

Eddington A. S., 1926, The Internal Constitution of the Stars. Cambridge Univ. Press, Cambridge

Emerson J., McPherson A., Sutherland W., 2006, The Messenger, 126, 41

Feast M. W., Catchpole R. M., 1997, MNRAS, 286, L1

Freedman W. L., Wilson C. D., Madore B. F., 1991, ApJS, 24, 14

Fricke K., Stobie R. S., Strittmatter P. A., 1972, ApJ, 171, 593

Gaia Collaboration, 2018, A&A, 616, A1

Gallenne A., Kervella P., Mérand A., Pietrzyński G., Gieren W., Nardetto N., Trahin B., 2017, A&A, 608, A18

Gieren W. P., Moffett T. J., Varnes T. G., 1999, ApJ, 512, 553

González-Fernández C. et al., 2018, MNRAS, 474, 5459

Hindsley R., Bell R. A., 1986, PASP, 98, 881

Jacyszyn-Dobrzeniecka A. M. et al., 2016, Acta Astron., 66, 149

Keller S. C., Wood P. R., 2006, ApJ, 642, 834

Kervella P. et al., 2017, A&A, 600, A127

Luck R. E., Moffett T. J., Barnes T. G. III, Gieren W. P., 1998, AJ, 115, 605

Madore B. F., 1982, ApJ, 253, 575

Marconi M., Clementini G., 2005, AJ, 129, 2257

Marconi M. et al., 2013, ApJ, 768, L6

Marconi M. et al., 2017, MNRAS, 466, 3206

Marengo M. et al., 2010, ApJ, 725, 2392

Milone A. P., Marino A. F., D'Antona F., Bedin L. R., Da Costa G. S., Jerjen H., Mackey A. D., 2016, MNRAS, 458, 4368

Molinaro R., Ripepi V., Marconi M., Bono G., Lub J., Pedicelli S., Pel J. W., 2011, MNRAS, 413, 942

Molinaro R. et al., 2012, ApJ, 748, 69

Moretti M. I. et al., 2014, MNRAS, 437, 2702

Moretti M. I. et al., 2016, MNRAS, 459, 1687

Muraveva T. et al., 2015, ApJ, 807, 127

Muraveva T. et al., 2018, MNRAS, 473, 3131

Nardetto N. et al., 2017, A&A, 597, A73

Neilson H. R., Langer N., Engle S. G., Guinan E., Izzard R., 2012, ApJ, 760, L18

Pietrzyński G. et al., 2013, Nature, 495, 76

Ripepi V., Moretti M. I., Clementini G., Marconi M., Cioni M. R., Marquette J. B., Tisserand P., 2012a, APSS, 341, 51

Ripepi V. et al., 2012b, MNRAS, 424, 1807

Ripepi V. et al., 2014, MNRAS, 437, 2307

Ripepi V. et al., 2015, MNRAS, 446, 3034

Ripepi V. et al., 2016, ApJS, 224, 21

Ripepi V. et al., 2017, MNRAS, 472, 808

Romaniello M. et al., 2008, A&A, 488, 731

Soszyński I., Udalski A., Szymański M. K., Kubiak J., Pietrzyński G., Wyrzykowski Ł., Ulaczyk K., Poleski R., 2010, Acta Astron., 60, 165

Soszyński I. et al., 2015, Acta Astron., 65, 297

Stobie R. S., 1969, MNRAS, 144, 511

van der Marel R. P., Cioni M.-R. L., 2001, AJ, 122, 1807

This paper has been typeset from a TEX/LATEX file prepared by the author.